A&A 421, 571–581 (2004)
DOI: 10.1051/0004-6361:20034377

Astronomy & Astrophysics

Magnetic fields in barred galaxies

III. The southern peculiar galaxy NGC 2442

J. Harnett[1,3], M. Ehle[2], A. Fletcher[3], R. Beck[3], R. Haynes[4], S. Ryder[5], M. Thierbach[3], and R. Wielebinski[3]

[1] University of Technology Sydney, PO Box 123, Broadway 2007, NSW, Australia
[2] XMM-Newton Science Operations Centre, European Space Agency, Villafranca, PO Box 50727, 28080 Madrid, Spain
[3] Max-Planck-Institut für Radioastronomie, Auf dem Hügel 69, 53121 Bonn, Germany
[4] University of Tasmania, GPO Box 252-21, Hobart 7001, Tasmania, Australia
[5] Anglo-Australian Observatory, PO Box 296, Epping, NSW 1710, Australia

Received 23 September 2003 / Accepted 3 April 2004

Abstract. Observations of the southern peculiar galaxy NGC 2442 with the Australia Telescope Compact Array in total and linearly polarized radio continuum at λ6 cm are presented and compared with previously obtained Hα data. The distribution of polarized emission, a signature of regular magnetic fields, reveals some physical phenomena which are unusual among spiral galaxies. We find evidence for tidal interaction and/or ram pressure from the intergalactic medium compressing the magnetic field at the northern and western edges of the galaxy. The radial component of the regular magnetic field in the northern arm is directed away from the centre of the galaxy, a finding which is in contrast to the majority of galaxies studied to date. The oval distortion caused by the interaction generates a sudden jump of the magnetic field pattern upstream of the inner northern spiral arm, similar to galaxies with long bars. An unusual "island" of strong regular magnetic field east of the galaxy is probably the brightest part of a magnetic arm similar to those seen in some normal spiral galaxies, which appear to be phase-shifted images of the preceding optical arm. The strong magnetic field of the "island" may indicate a past phase of active star formation when the preceding optical arm was exposed to ram pressure.

Key words. magnetic fields – polarization – turbulence – ISM: magnetic fields – galaxies: individual: NGC 2442

1. Introduction

More than twenty years of observations and modelling have shown that large-scale, or regular, magnetic fields pervade the interstellar medium in all spiral galaxies (Beck 2000, 2002). Observing linearly polarized radio emission is a well-established method for investigating the strength and structure of such regular magnetic fields, which are often controlled by the dynamics of the interstellar gas.

Large-scale magnetic fields in spiral galaxies lie predominantly in the plane of the discs. In normal (i.e. "non-barred") spirals, the morphology is usually qualitatively similar to the optical appearance of the host galaxy except that the strongest regular fields often lie in the inter-arm regions (Beck & Hoernes 1996). These "magnetic arms" may be caused by enhanced magnetic diffusion in the optical arms (Moss 1998) and/or by enhanced dynamo action in the inter-arm regions (Rohde & Elstner 1998; Shukurov 1998).

Send offprint requests to: J. Harnett,
e-mail: jules@eng.uts.edu.au

The presence of a stellar bar in a spiral galaxy, on the other hand, results in highly non-circular motions of the gas and stars in a galaxy. Strong deflection of gas streamlines along shock fronts in the bar region and significant compression of the gas have been predicted by Athanassoula (1992), Piner et al. (1995), Lindblad et al. (1996) and Englmaier & Gerhard (1997). Gas in the bar region rotates faster than the bar pattern itself and compression regions develop, traced by dust lanes. This gas inflow is hard to observe spectroscopically. In addition, the processes involved are likely to be interdependent as collisions of dense gas clouds and shocks in the bar potential may be modified by strong, regular magnetic fields. Theoretical models have recently begun to address the relationship between magnetic fields and gas flows in barred spirals (Moss et al. 2001).

Radio observations of the SBc galaxy NGC 1097 indicate that the regular magnetic fields in barred galaxies differ markedly from those we see in non-barred galaxies (Beck et al. 1999). Instead of exhibiting an open spiral pattern that is qualitatively similar to the optical morphology, the regular field appears to be tightly bound to the local gas flow in the bar.

Table 1. Properties of NGC 2442.

Parameter	
Right ascension (J2000)	$07^h36^m23^s.9$
Declination (J2000)	$-69°31'50''$
Type	SBbc(rs) II
Major diameter D_{25} ($'$)	5.5
Distance (Mpc)	15.5[1]
Inclination (0° is face on)	24°[2,3]
PA of major axis	40°[2]

[1] Ryder et al. (2001).
[2] Bajaja et al. (1999). However, Ryder (1995) argues that the galaxy is more highly inclined.
All other data are from de Vaucouleurs et al. (1991).

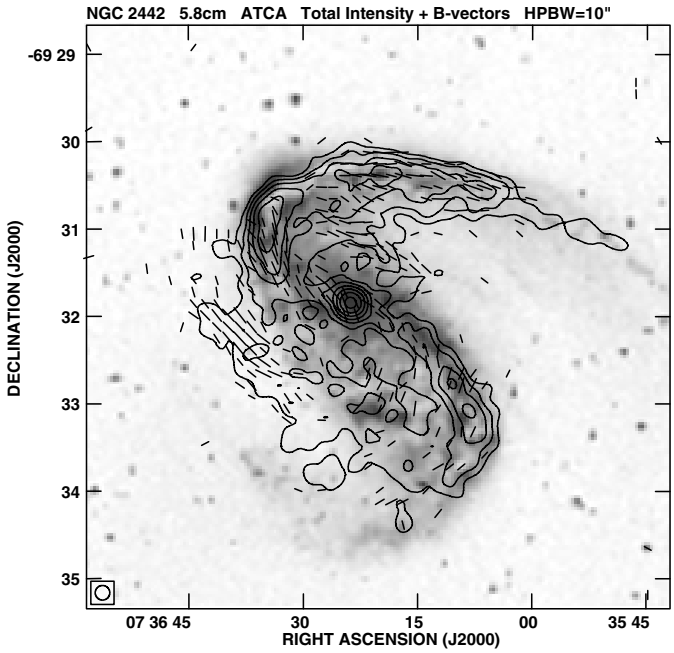

Fig. 1. NGC 2442: total λ6 cm emission shown as contours overlaid on a greyscale image from the DSS. The half-power width (*HPBW*) of the synthesized beam is 10″. Contours are 1, 2, 4, 8, 16, 32, 64× the basic contour level of 10^{-1} mJy/beam. Straight lines are ***E***-vectors rotated by 90°, not corrected for Faraday rotation, lengths scale with polarized emission and 1″ represents 10^{-2} mJy/beam.

Gas inflow along the compression region may fuel star formation in a dense, inner, circum-nuclear ring, which is also delineated by enhancement of the total, mostly turbulent magnetic field. In the circum-nuclear ring regular magnetic fields appear spiral in shape and so they probably decouple from the gas flow. As a result, the regular magnetic fields may facilitate angular momentum transfer which results in funnelling of the circum-nuclear gas toward the active nucleus.

We have undertaken radio continuum observations of 20 barred galaxies with the Effelsberg 100 m telescope, the Very Large Array (VLA) operated by the NRAO[1] and the Australia Telescope Compact Array (ATCA)[2]. As this project consisted of the first systematic search for magnetic fields in barred spiral galaxies, we chose a sample of galaxies with prominent optical bars. Ten of the galaxies were observed with the VLA and Effelsberg telescopes, the rest with the ATCA telescope. We are continuing our research into the magnetic fields and dynamic processes in the circum-nuclear regions of barred galaxies with detailed observations of a sub-sample of the original galaxies. Details are given by Beck et al. (2002).

In this paper, we discuss the southern peculiar galaxy NGC 2442.

2. NGC 2442

Basic information about NGC 2442 is given in Table 1. Following Ryder et al. (2001), we use a distance of 15.5 Mpc, at which 1″ corresponds to 75 pc along the major axis and 82 pc along the minor axis.

The striking appearance of NGC 2442 (see Fig. 1) is predominantly due to the deformed outer spiral arms so that the inner spiral arms look like a huge bar in the NE–SW direction. The true bar, leading to the galaxy's optical classification (de Vaucouleurs et al. 1991), is a small feature running *EW*, ∼66″ (5.0 kpc) long, centred on the nucleus. According to Bajaja et al. (1995, 1999) and Mihos & Bothun (1997) there is also a weak, elliptical circum-nuclear ring of molecular gas and star formation that has the same major axis orientation as the bar and a radius of ∼12.″5.

Two spiral arms emerge from the ends of the bar and proceed symmetrically along the NE–SW direction for ∼2′, but then become completely asymmetric. The northern arm is well-developed, but elongated and bisected by a prominent dust lane. It is bent back on itself by over 90°. The southern arm is less conspicuous, broader and traversed by many apparently chaotic dust lanes (see Fig. 1), and bends by about 180° towards the northeast, reaching the left edge of Fig. 1.

The distorted morphology hints at recent tidal interaction or ram pressure stripping as the galaxy traverses the intra-cluster medium (Mihos & Bothun 1997; Ryder et al. 2001). Imprints of non-circular rotation are evident from the velocity field, especially around the northern spiral arm (Bajaja et al. 1999; Houghton 1998).

Recent work referred to by Ryder et al. (2001) has shown that the group of galaxies in Volans associated with NGC 2442 contains more than the three other galaxies originally named by Garcia (1993): NGC 2397, NGC 2434, and PGC 20690. The perpetrator of the alleged interaction, however, remains unclear, particularly in view of the discovery of a large gas cloud with obvious streaming structures, HIPASS J0731–69, apparently associated with NGC 2442 and extended to the north and west (Ryder et al. 2001).

Earlier observations in H I (Bajaja & Martin 1985) provided mass and systemic velocity estimates, while ^{12}CO(1–0)

[1] The National Radio Astronomy Observatory is a facility of the National Science Foundation operated under cooperative agreement by Associated Universities, Inc.
[2] The Australia Telescope Compact Array is part of the Australia Telescope which is funded by the Commonwealth of Australia for operation as a National Facility managed by CSIRO.

Table 2. Observational data at λ6 cm (5170 MHz) for NGC 2442.

Date	Configuration	Time on source (h)
1996 Jan. 19	750C	3
1996 Feb. 9 + 11	750B	4
1996 Nov. 2	750A	10
1998 Mar. 25	375	9
2000 Dec. 31	750C	11

observations with SEST (Harnett et al. 1991; Bajaja et al. 1995) provided the velocity field of the molecular gas.

The ^{12}CO(1–0) distribution correlates remarkably well with the Molonglo Observatory Synthesis telescope (MOST) λ35 cm emission presented by Harnett (1984). Both SEST and the MOST have angular resolutions ~43″. ATCA images in H I and λ20 cm continuum (Houghton 1998) also posses similar morphological characteristics except that H I is weak in the galaxy's centre.

Between 5 GHz and 408 MHz, the radio spectral index is $\alpha = -0.92 \pm 0.08$ ($S \propto \nu^{\alpha}$) (Harnett 1984); this indicates that the dominant radio continuum emission mechanism is synchrotron radiation rather than thermal processes.

3. Observations and data reduction

In the continuum observation mode at the ATCA, data are acquired in two independent linear polarizations. The standard ATCA primary flux density calibrator J1934–638 was observed at the start and end of each synthesis observation and secondary (phase) calibrators were observed regularly to give good parallactic angle coverage. In Table 2 we present particulars of the λ6 cm ATCA observations of NGC 2442.

The *MIRIAD* data reduction package (Sault & Killeen 1998) was used for data reduction. Each data set of total bandwidth 128 MHz and 32 channels was edited and calibrated separately, data from all observations were then combined and reduced in the standard way (Ehle et al. 1996; Sault & Killeen 1998). Images shown here were made excluding 6-km baseline data.

Stokes Q and U parameter maps were used with the *MIRIAD* polarization software to generate images of linearly polarized intensity (*PI*, corrected for positive bias) and position angle (PA). The final maps of total and polarized intensities at 10″ resolution are shown in Figs. 1 and 2.

We also obtained data for NGC 2442 at λ13 cm from the ATCA. Details are given in Beck et al. (2002). The map of total intensity at λ13 cm suffers severely from missing short spacings as only the 1.5 km array configuration was used, whereas the λ6 cm observations utilised both the 750 m and 375 m arrays. Polarized intensity is weak at λ13 cm; significant signal-to-noise ratios are reached only after smoothing to 45″ (Fig. 4).

With only one total intensity map at high angular resolution, we were unable to separate the thermal and non-thermal (synchrotron) emission components. The typical average thermal fraction in spiral galaxies at λ6 cm is ≃20% (e.g. Niklas et al. 1997), but may locally reach ≃50% in star-forming regions.

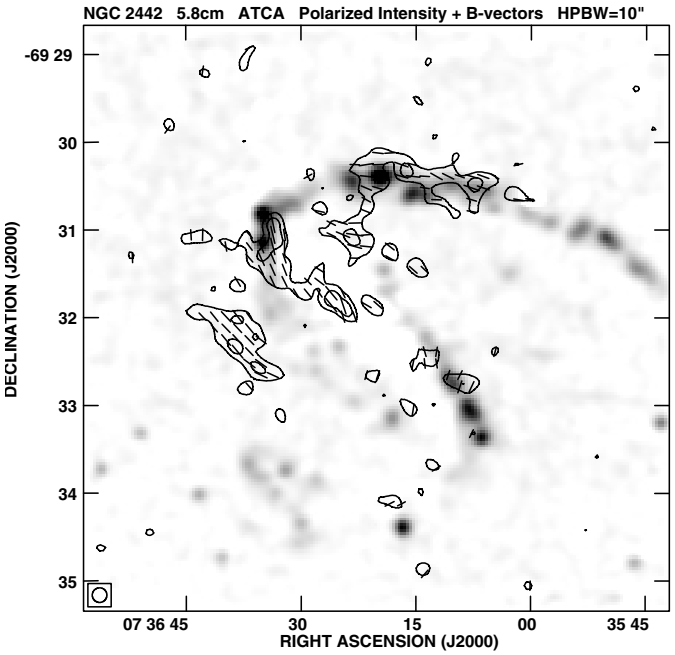

Fig. 2. NGC 2442: polarized emission at λ6 cm shown as contours overlaid on a greyscale image of Hα emission. The half-power width (*HPBW*) of the synthesized radio beam is 10″ and the Hα image has been smoothed to this resolution. Contours are 3, 5 × the basic contour level of 25 μJy/beam. Straight lines are ***E***-vectors rotated by 90°, not corrected for Faraday rotation, lengths vary with polarized emission and 1″ represents 10 μJy/beam.

For comparison with the radio images, we made a continuum subtracted H α map (see Fig. 2) using observations of NGC 2442 by Ryder & Dopita (1993), smoothed to a resolution of 10″.

4. Results

In Fig. 1 we present the total λ6 cm continuum emission from NGC 2442 as a contour plot with ***B***-vectors (the observed orientation of the electric polarization vector rotated by 90°, without correction for Faraday rotation), their lengths proportional to the polarized intensity, overlaid on a Digital Sky Survey (DSS) image. The restoring *HPBW* is 10″. The integrated total flux density within a radius of 3′ is $S = 123 \pm 12$ mJy and the integrated polarized intensity (Fig. 2) is 20 ± 5 mJy, giving an overall degree of polarization of 16 ± 4%. Both images have an rms noise 25 μJy/beam. The total flux density is significantly higher than the 74 ± 4 mJy reported by Beck et al. (2002), probably due to a baseline error in the earlier map. Using a λ6 cm flux density of 80 ± 10 mJy, Harnett (1984) derived a spectral index of $\alpha = -0.92$ ($S \propto \nu^{\alpha}$) for NGC 2442 – unusually steep for spiral galaxies (Condon 1992). The higher flux density determined using our new λ6 cm map is compatible with a flatter spectral index of $\alpha \simeq -0.75$, more typical for spiral galaxies.

The total intensity arms are noticeably wider than the Hα arms shown in greyscale in Fig. 2, a clear indication that much of the radio continuum emission is non-thermal and that cosmic ray electrons diffuse a long way from their presumed sources in supernova remnants. In general, the structure

in total intensity mimics the large-scale optical morphology to at least the 40 μJy/beam level. Emission from the deformed spiral arms and the nuclear region, where the peak intensity of 8.8 mJy/beam occurs, are all apparent in Fig. 1. The small optical bar is barely visible. There is no circum-nuclear ring in radio continuum, even with our best angular resolution of 10″. The most striking aspect of the emission is the steep gradient at the outer edge of the prominent northern arm. In the following, we will call the extended northern arm the "peninsula". Here the emission runs parallel and close to the well-delineated dust lane. There is also a local maximum of 2.0 mJy/beam at RA $07^{h}36^{m}20^{s}$, Dec $-69°30'30''$, that appears to coincide with two optically prominent H II complexes. Diffuse emission also extends to the west and south in the region enclosed by the northern arm, where no optical counterpart is apparent. We will call this area around RA $07^{h}36^{m}20^{s}$, Dec $-69°31'$ the "bay" in our discussion below.

In regions where spiral arms turn suddenly, theoretical models predict enhanced turbulence and velocity shear (Roberts et al. 1979; Athanassoula 1992; Lindblad et al. 1996). Increased star formation and tangling of magnetic field lines are expected to result in an increase in total synchrotron emission, but also lower the degree of polarization. We see some evidence of this at the ∼90° bend in the northern arm, where strong Hα emission and strong total radio emission of up to 2 mJy/beam is detected, whilst the linearly polarized component rapidly disappears (see Figs. 1 and 2).

South of the nucleus, the λ6 cm image (Fig. 1) reveals extended, smooth emission from the less well-defined southern arm, with local maxima and a sharp western edge. To the southeast, the emission follows the faint southern spiral arm after it has turned. There is a local maximum near to the turn itself. Only small patches of polarized emission are detected near the southern arm (Fig. 2).

No enhanced emission was detected from the position of SN1999ga – RA $7^{h}36^{m}17^{s}$, Dec $-69°33'22''$ (Woodings et al. 1999).

First seen in the MOST images (Harnett 1984), significant large-scale non-thermal emission to the east is visible in Fig. 1, without any optical or Hα counterpart. The extremely high degree of polarization makes this feature prominent in polarized intensity (Fig. 2). In the following, we will refer to this feature as the "island" (see Sect. 5.4). Note that none of the three regions – the peninsula, the bay and the island – are artifacts of resolution (compare Figs. 2 and 3).

The orientations of the ***B***-vectors and the extent of the polarized emission are presented in Fig. 2 as overlays on an Hα image. The large-scale regular magnetic field is patchy with maximum extent along the peninsula; note that the ridge of polarization along the peninsula is clearly shifted to the outside of the Hα arm. From the regions of enhanced turbulence, where the arms turn suddenly and strong wavelength-independent depolarization is expected to occur, the polarized emission from the northern arm abruptly weakens. No polarized emission was detected from the turn in the southern arm. Generally in the southern arm, only weak polarized emission is evident. We detected some diffuse polarized emission after smoothing (see Figs. 3 and 4). Figure 3 shows the orientation

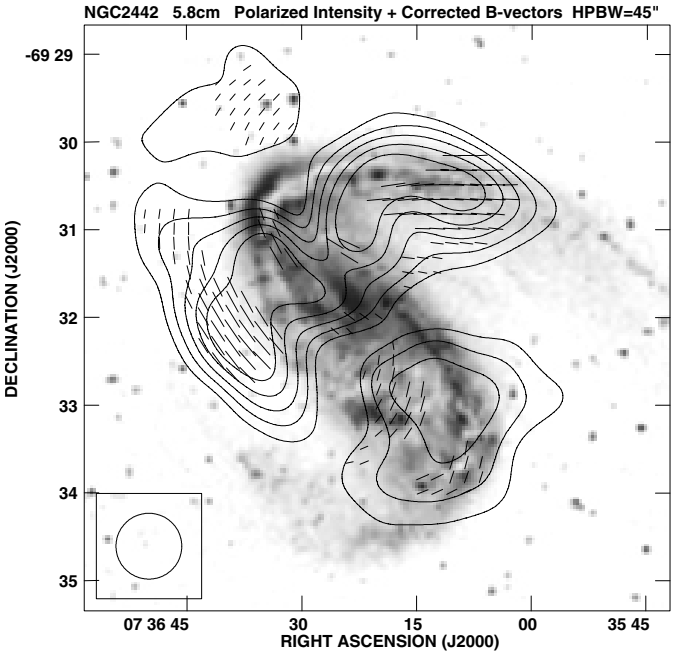

Fig. 3. NGC 2442: polarized emission at λ6 cm shown as contours overlaid on a greyscale image from the DSS. The half-power beam width (*HPBW*) is 45″. Contours are 1, 1.5, 2, 2.5, 3, 3.5 × the basic contour level of 4×10^{-2} mJy/beam. Straight lines are ***E***-vectors rotated by 90° and corrected for Faraday rotation, thus showing the orientation of the plane-of-sky regular component of the magnetic field in NGC 2442. The lengths of the "vectors" vary with polarized emission and 1″ represents 63 μJy/beam.

of the plane-of-sky component of the regular magnetic field in NGC 2442, obtained by rotating λ6 cm ***E***-vectors by 90° and correcting for the effects of Faraday rotation (Fig. 5). The regular field is thought to lie predominantly in plane of most disc galaxies (Beck et al. 1996), in which case Fig. 3 shows the intrinsic orientation of the regular magnetic field in NGC 2442. Note that Fig. 3 has been generated by smoothing the λ6 cm polarized emission (displayed in Fig. 2) by a factor of 4.5 to match the angular resolution at λ13 cm (Fig. 4). The corrected vectors are plotted only where polarized emission at both wavelengths is above 3× the noise level.

The best-aligned and strongest regular fields are located along the inner northern arm, the peninsula, and at the island and the bay. In the peninsula, the vectors are coherent over ∼90″ ≃ 7 kpc and are generally oriented parallel to the dust lane, which may be a sign of a large-scale shock (see Sect. 5.3.1).

Faraday rotation measures (*RM*) between λ6 cm and λ13 cm are shown in Fig. 5 at a resolution of 45″ (no correction for Faraday rotation due to the Milky Way foreground has been applied). Two large, coherent patches of *RM* are visible: at the position of the island, where $18 < RM < 27\,\mathrm{rad\,m^{-2}}$, and at the peninsula, where $-60 < RM < -35\,\mathrm{rad\,m^{-2}}$. The smooth variation and constant sign of the *RM*s in these two patches means that the magnetic field has a coherent, uni-directional regular component (see e.g. Beck et al. (1996) for more details on Faraday rotation and galactic magnetic fields).

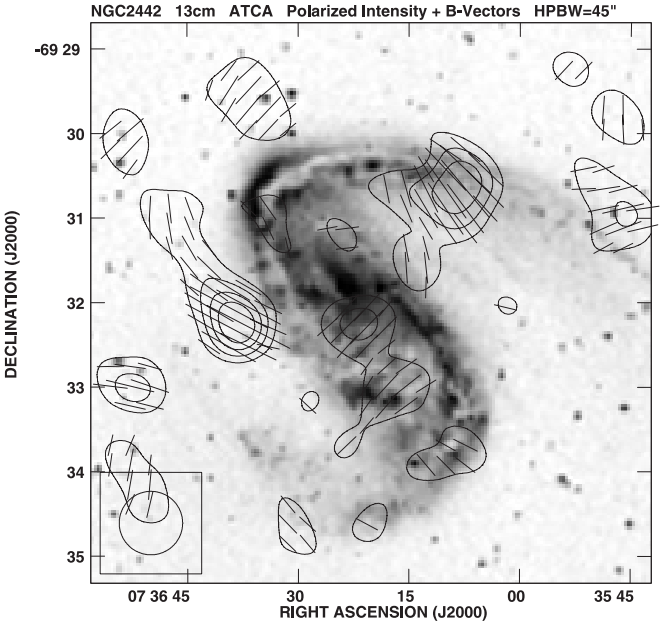

Fig. 4. NGC 2442: polarized emission at λ13 cm emission shown as contours overlaid on a greyscale image from the DSS. The half-power beam width (*HPBW*) is 45″. Contours are 1, 2, 4, 8, 12, 16, 32, 64 × the basic contour level of 7×10^{-2} mJy/beam. Straight lines are ***E***-vectors rotated by 90°, lengths vary with polarized emission and 10″ represents 5×10^{-2} mJy/beam.

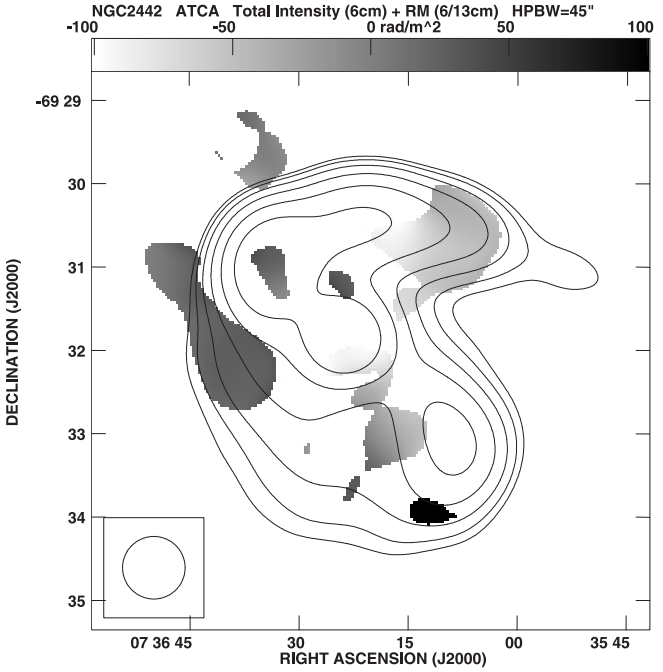

Fig. 5. NGC 2442: rotation measures between λ13 cm and λ6 cm shown as a greyscale image with contours representing the total λ6 cm emission with a *HPBW* of 45″. Contour levels are 1, 2, 4, 8, 12, 16, 32 × the basic contour level of 2×10^{-1} mJy/beam.

The different signs of *RM* in the island and peninsula seem to indicate that the regular field is pointing in different directions. However, the island is located near the minor axis (which has a position angle of 130°) of the projected galaxy plane where any plane-parallel, predominantly azimuthal, regular field has only a small line-of-sight component. Hence, we suspect that the positive *RM* in the island is due to the foreground plasma in the Milky Way; indeed, values around $+20\,\mathrm{rad\,m^{-2}}$ are consistent with the foreground *RM* expected near Galactic coordinates $l \simeq 280°, b \simeq -20°$ (Han et al. 1997). If so, the measured *RM*s from the peninsula are also affected by the foreground *RM* and the intrinsic values in fact are $-90 \lesssim RM \lesssim -55\,\mathrm{rad\,m^{-2}}$. Assuming trailing spiral arms, we learn from the velocity field (Bajaja et al. 1999) that the north-western side with the peninsula is the far side of the galaxy. This means that the radial component of the regular magnetic field is directed away from the centre of the galaxy (if we assume that the regular field lies predominantly in the plane of the galaxy), in contrast to the majority of galaxies studied so far (Krause & Beck 1998).

5. Magnetic field properties

5.1. Asymmetry of λ6 cm emission

To investigate the symmetry of the emission in NGC 2442, we have averaged the flux density in two regions separated by the minor axis. The intense emission all along the northern arm results in a strong asymmetry in total intensity. We find the north/south ratio of polarized λ6 cm flux densities in the two regions to be, rather surprisingly, only 1.6 compared to 3.4 for the total emission. While the polarized emission shows distinct features only in the northern half, there is weak diffuse polarized emission in the southern half (Fig. 3).

5.2. Local magnetic field strengths

Table 3 lists the mean total, non-thermal and polarized intensity as well as the magnetic field properties of the island, inner northern arm at the turning point, peninsula and bay. The total magnetic field strength B_{tot} is estimated assuming energy equipartition between cosmic ray particles and the magnetic field (e.g. Longair 1994, p. 292). The strength of the regular magnetic field B_{reg} is derived from the degree of polarization. The following assumptions are used: the depth of the emitting layer is 1 kpc, the ratio of the energies present in relativistic protons to electrons is 100, the low energy cutoff for cosmic ray protons is 300 MeV, and the synchrotron spectral index is $\alpha \simeq -0.9$ (Harnett 1984). We integrate over a fixed energy interval in the cosmic-ray spectrum to obtain the total energy density of the cosmic rays independent of the magnetic field strength (see Beck 2000). The thermal fraction in the spiral arms and the bay is assumed to be 30%, but the emission from the island at λ6 cm is taken to be completely non-thermal, as indicated by the high percentage of polarized emission and absence of Hα emission. Most of these assumptions are canonical, based on estimates for the Milky Way and a few other galaxies, and are clearly subject to large errors. The derived magnetic field strength is proportional to the power $(3-\alpha)^{-1} \simeq 1/4$, so even large uncertainties cause only small errors in the deduced field strength; we estimate typical errors of ±30%.

Table 3. Total power, polarized intensity and equipartition magnetic field strengths in NGC 2442.

	Island	Northern arm at turn	Peninsula	Bay
Mean total intensity (μJy/beam)	198 ± 23	1606 ± 22	593 ± 22	271 ± 17
Mean non-thermal intensity (μJy/beam)	198 ± 23	1166 ± 22	415 ± 22	68 ± 17
Mean polarized intensity (μJy/beam)	102 ± 23	87 ± 22	77 ± 22	101 ± 17
Percentage polarized emission	52 ± 13%	7 ± 2%	19 ± 5%	36 ± 9%
Total magnetic field strength (μG)	16 ± 5	26 ± 8	20 ± 6	16 ± 5
Regular magnetic field strength (μG)	13 ± 4	7 ± 2	9 ± 3	10 ± 3

Notes: errors in radio emission intensities are the rms noise weighted by the area over which the average emission was calculated; errors in equipartition magnetic field strengths are estimated to be 30% (see the text for details).

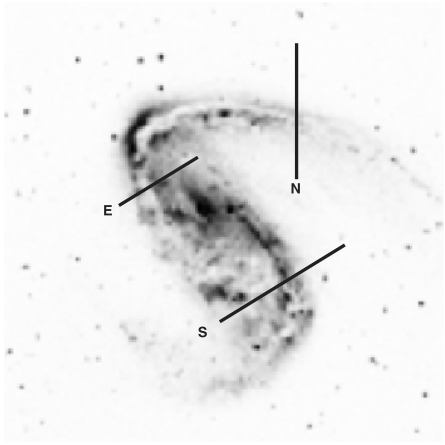

Fig. 6. NGC 2442: DSS image of NGC 2442 showing positions of slices discussed in the text. The position of the label on each slice shows the left end of the x-axis in Figs. 7–9.

The total magnetic field strength is high in the northern spiral arm, probably as a result of stronger driving of interstellar turbulence by, for example, star formation and gravitational instabilities. The very highly polarized emission in the island and bay means that the field here is mostly regular. If the equipartition assumption is valid, the regular magnetic field strength estimates of $B_{\rm reg} \simeq 13\,\mu$G are very high, comparable to $B_{\rm reg}$ in the magnetic arms of NGC 6946 (Beck 1996).

5.3. Comparison of total and polarized radio emission at λ6 cm

In Fig. 6, we show the positions of slices through the arms of NGC 2442, that we used to compare the emission in total power, polarized emission, infrared K-band (Ryder unpublished) and Hα. We found that the K-band and Hα have similar normalized profiles and therefore we only present Hα data. For each slice, the position of the label denotes the left end of the x-axis in Figs. 7–9.

Before making the slices "N" and "S" we smoothed the radio and Hα maps at original resolution ($10''\times10''$) with a highly elliptical, $10''\times30''$ beam, with the major axis of the smoothing beam oriented parallel to the local direction of the arm. This has a similar effect to averaging several neighbouring slices, and so reduces the risk of developing an interpretation of the emission profiles based on an atypical slice. As a further check we made more slices through the original maps, not shown here, and found that the cross-section obtained following smoothing with an elliptical beam is a representative, average profile. The smoothing also increases the signal to noise ratio of any diffuse emission, especially in the weak southern arm, without losing resolution in the direction perpendicular to the arm. Slice "E" is based on the original unsmoothed map.

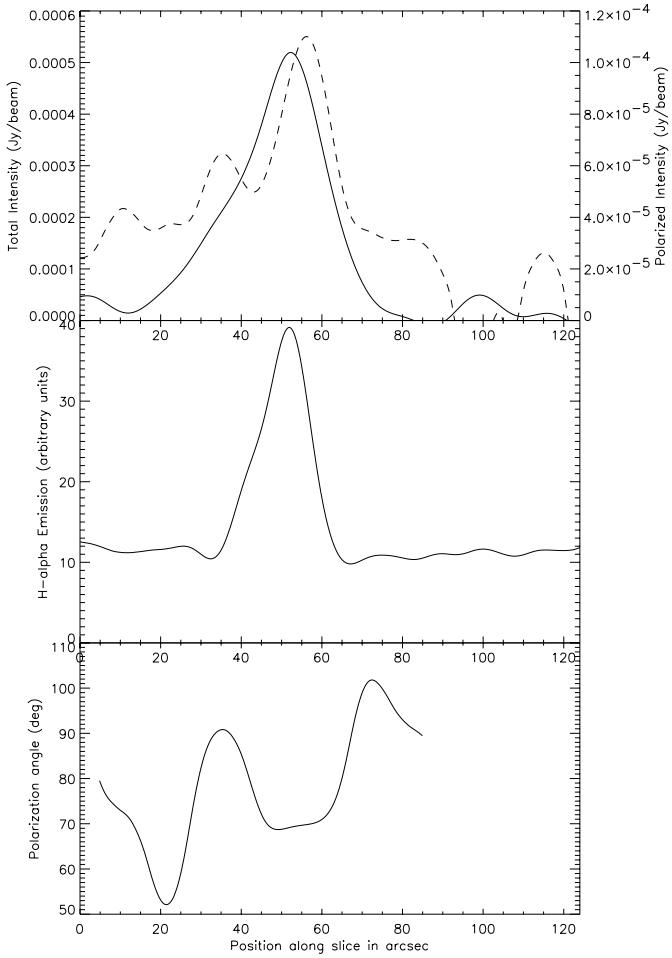

Fig. 7. Slice across the bay and the peninsula (position N in Fig. 6). South is to the left. *Upper panel*: total (solid line) and polarized (dashed line) λ6 cm emission, both smoothed to a beam of $10'' \times 30''$ oriented parallel to the spiral arm. *Middle panel*: Hα emission. *Bottom panel*: "***B***-vector" position angles.

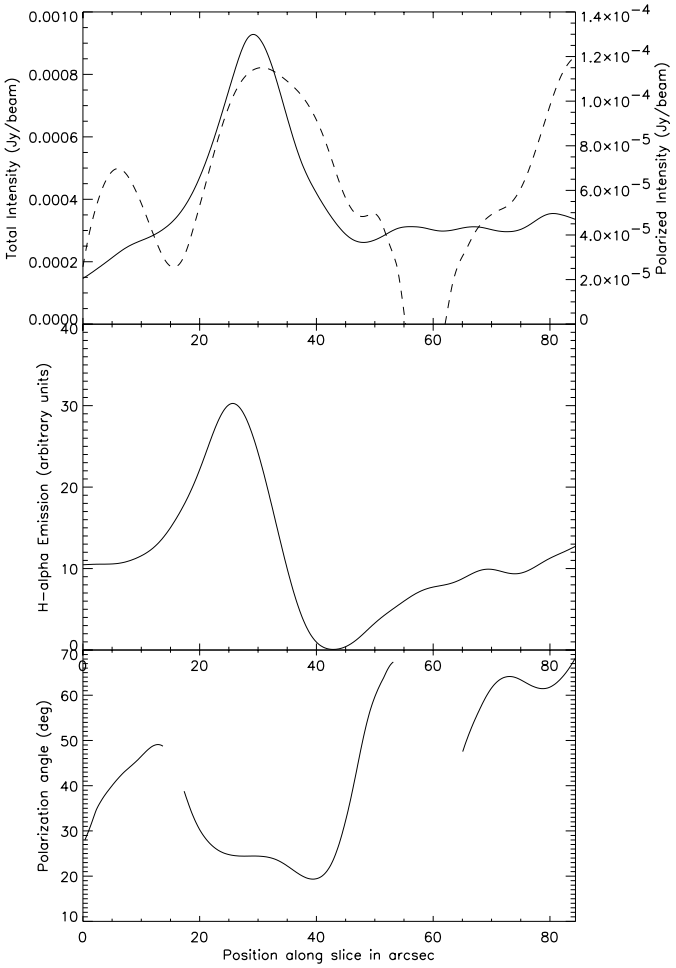

Fig. 8. Slice across the northern arm (position E in Fig. 6). East is to the left. *Upper panel*: total (solid line) and polarized (dashed line) λ6 cm emission, both at the original $10'' \times 10''$ resolution. *Middle panel*: Hα emission. Bottom panel: "***B***-vector" position angles.

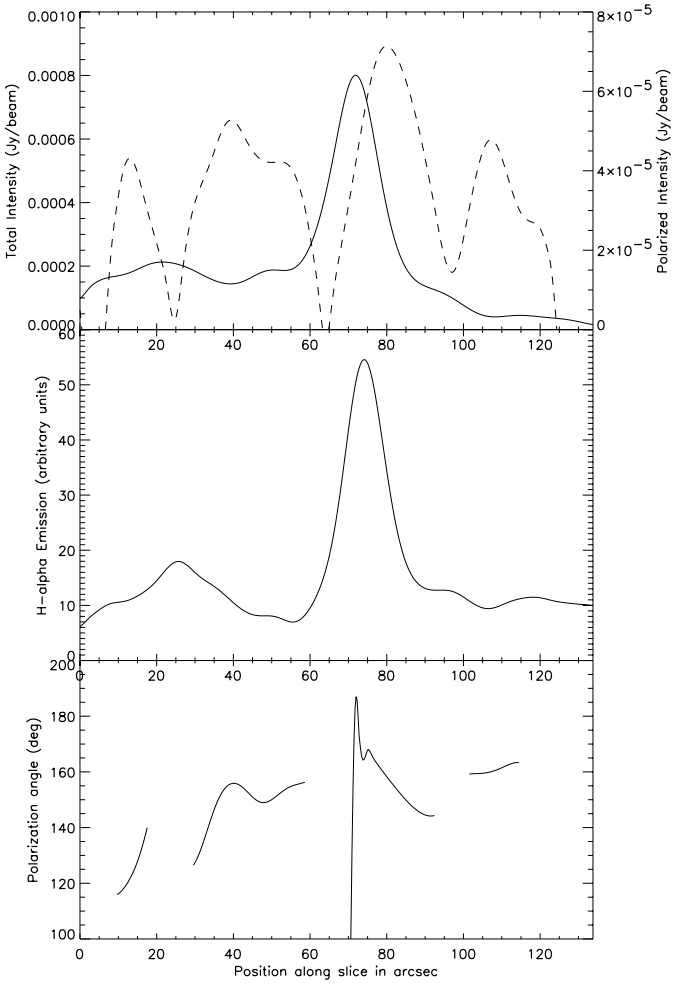

Fig. 9. Slice across the southern arm (position S in Fig. 6). East is to the left. *Upper panel*: total (solid line) and polarized (dashed line) λ6 cm emission, both smoothed to a beam of $10'' \times 30''$ oriented parallel to the spiral arm. *Middle panel*: Hα emission. *Bottom panel:* "***B***-vector" position angles.

5.3.1. The peninsula: Slice N

Figure 7 shows that whilst the profile of the strongest peak in polarized emission (*PI*) has an approximately Gaussian profile, the total power (*TP*) profile is asymmetric, broader and is displaced by $5''$ or approximately half a beam-width. As long as the signal to noise ratio of the peaks are sufficiently high this displacement is reliable *even though the shift is less than the beam-size* θ. To illustrate this, assume that the signal at a peak has a Gaussian profile $S_1 = S_0 \exp(-(x - x')^2/(\theta)^2)$ with amplitude S_0, centred on x' and that this signal is combined with random noise that serves to produce a second maximum within the beam $S_2 = N_0\delta(x - x')/\theta$, of amplitude N_0 shifted by a random factor δ from the true peak. Expanding S_1, adding S_1 to S_2 and differentiating gives an estimate for the positional accuracy of the peak Δx in terms of the beam-size θ and the signal to noise ratio S_0/N_0

$$\Delta x \simeq \frac{N_0\delta\theta}{2S_0} \sim \frac{\theta}{2S_0/N_0}, \quad (1)$$

where we conservatively assume that the noise has a maximum right at the edge of the beam (i.e. $\delta = 1$). With $TP = 500\,\mu$Jy, $\sigma_{TP} = 25\,\mu$Jy, $PI = 110\,\mu$Jy and $\sigma_{PI} = 25\,\mu$Jy at the peak in slice N, using Eq. (1) we expect the error in position of the *TP* peak to be $\pm 0.5''$ and that in *PI* to be $\pm 2''$.

Given the distance of 15.5 Mpc, the emission maxima are separated by ~400 pc. The peak of the Hα and *TP* profiles coincide exactly, but the former is narrower (Fig. 7, middle panel). We conclude that along this slice, the strongest total emission (comprising thermal + non-thermal emission) coincides with a region of significant star formation, as indicated by the Hα profile. This coincidence is in obvious contrast to the inner northern arm (Fig. 8) and indicates that the peninsula is not subject to density-wave compression, where a shift between the peaks of thermal and non-thermal emission is expected (Sect. 5.3.2).

The polarized emission and therefore the regular magnetic field is strongest toward the *outer* edge of the peninsula, i.e. to the north of the star-forming region (Fig. 7). This shift between the total and polarized emission could be due to Faraday depolarization within the northern arm. Intrinsic Faraday rotation measures between λ6 cm and λ13 cm are $\simeq -70$ rad m^{-2} in the peninsula (Sect. 4). Another estimate of the amount of

Faraday rotation is based on the variation of polarization angles (Fig. 7, bottom panel); the angles in the spiral arm, around the peak in total emission, are smaller by about 20° compared to the angles on either side, which corresponds to a Faraday rotation of $\simeq -90$ rad/m^2 and to very weak depolarization by differential Faraday rotation of 0.92 (see Sokoloff et al. (1998) for a detailed discussion of Faraday depolarization). This is insufficient to account for the difference in degree of polarization ($p = PI/TP$) between the peak in *TP*, where $p = 18\%$, and the peak in *PI*, where $p = 24\%$. Depolarization by Faraday dispersion in the turbulent magnetic field of the peninsula is another possibility. However, if the shift in the *PI* peak is a product solely of depolarization in a thermal plasma, we would expect the *PI* profile to be symmetric about the Hα profile. In other words, there should be a *PI* minimum in the peninsula which is not the case.

Our favoured explanation for the displacement of the regular field is ram pressure exerted by the intergalactic medium. The velocity field is strongly distorted in the peninsula (Bajaja et al. 1999). Ram pressure would increase the strength of the magnetic field component perpendicular to the direction of the pressure and tend to turn the ***B***-vectors perpendicular to the streaming velocity of the intergalactic medium, which we assume to be roughly in the N–S direction. This agrees reasonably well with the observed position angles of the ***B***-vectors in this region of about 90°.

Highly polarized radio emission at the outer edges of spiral arms due to ram pressure was also detected in NGC 2276 (Hummel & Beck 1995) and in the Virgo galaxy NGC 4254 (Soida et al. 1996). Polarized emission is a very sensitive tracer of such compression effects.

Tidal interaction may be another reason for the distorted peninsula and its sharp outer edge, as demonstrated by N-particle models (e.g. Combes et al. 1988). Observations of H I by Houghton (1998) indicate gravitational disturbances in the velocity fields of two galaxies near to NGC 2442, [VC2]073649.1–691448 and ESO 059–G006. Ram pressure should compress H I gas along the outer edge of the peninsula, whilst no systematic shifts between gas, magnetic fields and star-forming regions are expected in tidal arms. Furthermore, tidal interaction can generate huge clouds of H I gas outside the spiral arms, but no such clouds were detected by Houghton (1998).

Another explanation is that slice N lies outside the co-rotation radius so that the pattern speed is faster than the speed of the gas orbits about the galactic centre. Star formation is triggered by the compression of the gas, where the arm catches up with it, i.e. to the north of the northern spiral arm. If the regular field were subsequently randomized by turbulence associated with these processes, we would expect the polarized emission to peak on the *outside* of the peninsula. In strongly barred galaxies the co-rotation radius lies at the ends of the bar. Although NGC 2442 has only a weak, short bar, it seems possible that the large-scale distortion of the spiral arms, particularly to the north-east, acts in the same way as a strong bar (Houghton 1998). To test the co-rotation assumption, we require velocity field data and accurate modelling of the pattern speed.

5.3.2. The inner northern arm: Slice E

The upper panel of Fig. 8 displays the profile of *TP* and *PI* in the direction E–W across the inner northern arm. Note that the map was not smoothed by an elliptical beam prior to making the slice; this method is only appropriate when the Stokes parameters I, Q and U are roughly constant in the direction perpendicular to the slice.

Here there is a slight displacement between the peaks in *TP* and *PI* emission. However, the *PI* peak is significantly broader than that in *TP* and the *PI* peak in slice "N". This indicates that the *PI* peak is not generated by a ram pressure or a density wave shock. The orientation of the ***B***-vectors (see lower panel of Fig. 8) jumps suddenly by ~40°, from ≃20° in the arm to ≃60° in the bay.

This situation is similar to that detected across the bar in NGC 1097 (Beck et al. 1999), where the regions of enhanced total emission (*TP*) coincide with the dust lanes along the bar, while the polarized emission is much broader and extends far into the upstream region. About 1 kpc upstream of the dust lane, the position angles of the ***B***-vectors change abruptly, which is indicated by a region of zero polarized intensity. Beck et al. (1999) conclude that a shear shock, due to the bar's gravitational potential, is responsible for both the deflection and amplification of the magnetic field.

We see an indication of such a field deflection in NGC 2442, but our resolution does not match that of the NGC 1097 image. We propose that a similar situation exists in NGC 2442 due to the bar-like distortion of the inner spiral arms. This means that the magnetic field along the "bar" aligns well with the local gas streamlines. We predict a sharp change in the velocity field profile.

The peak in Hα emission is shifted ≃5″ east, or downstream, of the *TP* peak. This offset is consistent with the interpretation that the gas at this radius rotates faster than the spiral pattern speed. In this case, gas and magnetic field are compressed when the gas enters the arm from the west, followed by star formation further downstream.

5.3.3. The southern arm: Slice S

Figure 9 shows a slice through the southern spiral arm marked S in Fig. 6. In this region, the *TP* emission is more extended and diffuse and the *PI* is patchy even after smoothing with a beam extended parallel to the arm. The position angles of the ***B***-vectors are roughly constant across the inner arm. There is an indication from our slice profile of the *PI* peak being shifted toward the *outer* edge, but the emission is very weak and patchy and may not be shaped by large scale processes. Nevertheless, both the sharp western edge of the spiral arm and the shift between the *PI* and *TP* peaks in Fig. 9 resemble the conditions in the peninsula (Fig. 7) and indicate that ram pressure may also act onto the southern arm.

5.4. The island

The island is displaced from the northern spiral arm by ~5 kpc – measured in the galaxy's plane – and is ~5.5 kpc

long in the high resolution map (Fig. 2). Here the continuum emission is strongly polarized, up to 50% of the total emission. There is no detected Hα counterpart.

Without star-forming activity the island probably does not contain the sources of the cosmic ray electrons producing synchrotron emission. Hence, the relativistic particles have to travel about 5 kpc, from the nearest star-forming regions, without significant energy losses. The timescale for synchrotron energy losses can be approximated by

$$t_{\rm e} \simeq \frac{8.35 \times 10^9 \ {\rm yr}}{\sqrt{\nu\,({\rm MHz})/16}\ (B_{\rm tot\perp}(\mu{\rm G}))^{1.5}}, \quad (2)$$

(Lang 1998, Sect. 1.25) where $B_{\rm tot\perp} \sim B_{\rm tot}$ is the plane-of-sky component of the total magnetic field. The streaming velocity, and hence the diffusion timescale, for the cosmic ray electrons is thought to depend on scattering of the particles by plasma waves. Avoiding complications, such as the statistical nature of interstellar turbulence and the magnetic field geometry, we make a crude assumption that the electrons stream at the Alfvén speed $v_{\rm A} = B_{\rm tot}/2\sqrt{\pi\rho}$ where ρ is the mass density of the fully ionised gas (e.g. Longair 1994, Sect. 20.4), and so the diffusion timescale to reach the island is

$$t_{\rm d} \simeq \frac{L}{v_{\rm A}}, \quad (3)$$

where L is the distance from the spiral arm to the island. For the cosmic ray electrons to reach the island before radiating away significant energy requires that $t_{\rm d} < t_{\rm e}$. Combining Eqs. (2) and 3 we obtain an upper limit on the product of the thermal electron density of the ISM and the magnetic field strength,

$$\sqrt{B_{\rm tot}(\mu{\rm G}) n_{\rm e}({\rm cm}^{-3})} \lesssim 0.21, \quad (4)$$

where we have assumed that the ISM is fully ionised hydrogen and $n_{\rm e}$ is the thermal electron density. For a total magnetic field strength between the northern arm and the island of $B_{\rm tot} \simeq 15\,\mu$G (similar to that in the bay), Eq. (4) gives an upper limit of $n_{\rm e} \lesssim 0.003\,{\rm cm}^{-3}$. Weaker magnetic fields or a denser ionised ISM would result in too slow an Alfvén speed for the cosmic ray electrons to reach the island, from their presumed sources near star forming regions.

If the cosmic ray electrons in the island are older than in the northern arm, their spectrum should steepen with distance from the places of origin. Unfortunately due to missing spacing problems at λ13 cm, we have only single-frequency information on the total intensity emission from NGC 2442. Our maps of polarized intensities cannot be used for spectral index studies because of wavelength-dependent depolarization mechanisms. Total intensity maps at other frequencies are needed.

Could the island be due to compression of the magnetic field? Compared to the compression feature in the peninsula, the island is too broad and, more importantly, on the "lee" side of the galaxy where no enhanced compression by ram pressure is expected or evident.

Could the island with its well-aligned vectors be the signature of a "magnetic arm" of the type seen between the optical arms of galaxies such as NGC 6946 (Beck & Hoernes 1996; Frick et al. 2000)? In Table 3 the estimated regular magnetic field strength is comparable to that of the magnetic arms in NGC 6946. The images at 45″ resolution (Figs. 3 and 4) show that the island extends to the north, indeed approaching the shape of a magnetic arm. Further, the $\boldsymbol{B}$-vectors in the smoothed λ6 cm map (Fig. 3) are oriented parallel to the inner northern spiral arm, even though they are ∼5 kpc downstream of the arm. This alignment can hardly be pure coincidence.

Another explanation, in view of the results presented above, is that the regular field is oriented with the $\boldsymbol{B}$-vectors parallel to shear motion in the tidal gas flow of the disturbed galaxy. The island might then represent a region of strong shear which enhances the magnetic field. The published velocity field (Bajaja et al. 1999) does not include the island region. Better data on Faraday rotation could test this possibility: sheared random magnetic fields generate strong polarized emission but little Faraday rotation whereas dynamo generated magnetic arms are strong in both quantities.

6. Conclusions

6.1. Summary of the observations

Our ATCA maps of the southern peculiar galaxy NGC 2442 in total and polarized intensity at λ6 cm and in polarized intensity at λ13 cm, in comparison with our new Hα map, reveal the following features:

- The spiral arms in total intensity are strongly deformed, like a large oval distortion, similar to the optical arms. The small optical bar is barely visible in radio continuum.
- The steep gradients in the radio emission at the northern and western edges indicate compression of the total magnetic field.
- Along the spiral arms, the peaks in total intensity agree well with those in Hα, but synchrotron emission makes the radio arm – and hence the magnetic field and cosmic ray distributions – broader than the Hα arm.
- The regular magnetic field has an unusual morphology and is concentrated along the outer northern arm (the "peninsula"), in the region enclosed by the northern arm (the "bay"), and in an "island" separated by about 5 kpc from the inner northern arm to the east.
- The regular magnetic field in the peninsula is systematically shifted outwards with respect to the spiral arms seen in total intensity and Hα by ∼400 pc. We interpret this as an indication of ram pressure exerted by the intergalactic medium.
- Across the inner northern arm, the orientation of the $\boldsymbol{B}$-vectors jumps suddenly by ∼40°. This behaviour is similar to a shear shock in the barred galaxy NGC 1097 (Beck et al. 1999), and indicates the presence of a major oval distortion of the gravitational field in NGC 2442.
- The highly polarized "island" is probably the peak of a magnetic arm between the two spiral arms, similar to the magnetic arms previously found in normal spiral galaxies. If magnetic arms are phase-shifted images of the preceding optical arm, the strong polarized emission from this feature

may reflect a phase of strong star formation about 10^8 yr ago, when the southern arm was exposed to ram pressure.
– The total magnetic field strength reaches 26 μG in the inner northern arm. The regular field strength in the island is $\simeq$13 μG. Both values are higher than is usual for spiral galaxies.

6.2. Some astrophysical implications

Our observations of NGC 2442 show that polarized radio emission is an excellent tracer of field compression due to interaction with the inter-galactic medium. Similar signatures of interaction have been identified in two other galaxies, NGC 2276 (Hummel & Beck 1995) and NGC 4254 in the Virgo Cluster (Soida et al. 1996).

The importance of the magnetic field to the distribution and dynamics of the ISM can be gauged by comparing the magnetic energy density to the energy density of the gas. In Sect. 5.2 we derived estimates of the total magnetic field strength of 16 μG in the "island" inter-arm region and 26 μG in the northern spiral arm, assuming equipartition between cosmic ray and magnetic field energy densities. These field strengths translate into energy densities of $U_{\rm B} \simeq 1$ and 3×10^{-11} erg cm^{-3}, respectively. The magnetic energy density in the arms is equivalent to that of neutral gas clouds with turbulent velocity 10 km s^{-1} and number density 35 cm^{-3}; this density is of the same order as the cold neutral medium in the Milky Way. (We are not aware of any measurements of local, neutral gas densities in the spiral arms of NGC 2442.) In the inner disc of NGC 6946 Beck (2004) determined the average density of the neutral gas to be 20 cm^{-3} and the turbulent energy density to be in equipartition with that of the magnetic field.

The importance of the magnetic field in the warm diffuse gas can be better estimated. Bajaja et al. (1999) found a temperature of $T \simeq 6500$ K and volume density of $n_{\rm e} \simeq 10$ cm^{-3} for a typical H II region in the northern arm of NGC 2442. The thermal energy density inside such a region is $U_{\rm th} \simeq 1\times10^{-11}$ erg cm^{-3}, giving a plasma $\beta = U_{\rm th}/U_{\rm B} \simeq 0.3$; the magnetic field may be important for the dynamics and morphology of H II regions. A similarly low value for β was derived for NGC 6946 (Beck 2004).

As the cosmic-ray electrons emitting in the island probably originate from the spiral arm and lose some fraction of their energy during their diffusion, the equipartition assumption gives a lower limit of the field strength in the inter-arm region. Such a strong field outside star-forming regions is exceptional and poses the question of the dynamical importance of the magnetic field. Little diffuse Hα emission is observed (Fig. 2; Mihos & Bothun 1997). We estimated an upper limit of $n_{\rm e} \simeq 0.003$ cm^{-3} in the "island" inter-arm region in Sect. 5.4, using the energy loss and diffusion timescales of cosmic ray electrons. Taking a canonical value of $T = 10^4$ K for the temperature of the diffuse gas we obtain $\beta \simeq 10^{-4}$: the magnetic field will be strongly dominant in the local dynamics of the inter-arm gas. However, note that the energy density associated with galactic rotation is several orders of magnitude higher than that of the magnetic field.

The radio emission from the island is highly polarized and so is clearly synchrotron radiation. But where do the cosmic ray electrons come from? There is no emission in Hα from this region, indicating no star formation. The timescale for synchrotron energy loss at λ6 cm in a 15 μG field is about 10^7 years (Eq. (2)) whereas a half rotation time – when this region would have been part of a spiral arm – is about 10^8 years (using $\simeq$250 km s^{-1} at 8 kpc radius, see Bajaja et al. 1999). The cosmic rays most probably originate in the spiral arms and travel at least 5 kpc in their lifetime. With an independent measure of the gas density, the quality of the assumption that the diffusion timescale of cosmic rays is proportional to the reciprocal of the Alfvén speed (Eq. (3)) could be tested against observations.

The origin of the $\sim$5 kpc long, ordered magnetic field in the island is not at all clear. Whereas the regular fields in the northern arm show strong signs that they are the result of compression of a tangled field, the inter-arm regular fields do not. Plausible mechanisms for producing strong, well ordered magnetic fields away from the spiral arms are enhanced dynamo action and shear arising from differential rotation of the gas disc. High-resolution observations of the velocity field, dynamo models and MHD models of the interaction are required to test this.

The images of polarized emission at 45″ resolution (Figs. 3 and 4) indicate that the island is the peak of a "magnetic arm", similar to that found in NGC 6946 (Beck & Hoernes 1996; Frick et al. 2000). The magnetic arms in NGC 6946 are phase-shifted images of the optical spiral arms preceding in the sense of rotation (Frick et al. 2000). Possible explanations are slow MHD waves (Fan & Lou 1997), where the waves in gas density and magnetic field are phase shifted, or enhanced dynamo action in the inter-arm regions (Moss 1998; Shukurov 1998; Rohde et al. 1999). In NGC 2442 the preceding gas arm to the east has a very small amplitude as seen in the H I observations of Houghton (1998). However, half a rotation ago ($\simeq 10^8$ yr, see above), this arm was fully exposed to the ram pressure of the intergalactic medium and, similar to the peninsula at present, probably had a much stronger amplitude in gas density. Star formation has ceased since then, but the magnetic field wave has survived. Hence, magnetic arms seem to preserve memory of the past phase of active star formation. Polarization observations with higher sensitivity and Faraday rotation measures at a higher resolution are needed to discriminate between the possible origins if the "island".

Acknowledgements. We thank Dmitry Sokoloff for helpful discussions and Elly M. Berkhuijsen and the referee for useful comments and carefully reading of the manuscript.
J.I.H. gratefully acknowledges the support and encouragement of the Alexander von Humboldt Society and the Max-Planck-Institut für Radioastronomie in Bonn, Germany, and in Australia of the University of Sydney and the Australia Telescope National Facility.
M.E. is grateful to the ATNF for providing support and facilities. His work in Australia was funded through grant No. Eh 154/1-1 from the Deutsche Forschungsgemeinschaft.
The Digitized Sky Survey was produced at the Space Telescope Science Institute under US Government grant NAG W-2166. The images of these surveys are based on photographic data obtained using the Oschin Schmidt Telescope on Palomar Mountain and the

UK Schmidt Telescope. The plates were processed into the present compressed digital form with the permission of these institutions.
This research has made use of the NASA/IPAC Extragalactic Database (NED) which is operated by the Jet Propulsion Laboratory, California Institute of Technology, under contract with the National Aeronautics and Space Administration.

References

Athanassoula, E. 1992, MNRAS, 259, 328
Bajaja, E., & Martin, M. C. 1985, AJ, 90, 1783
Bajaja, E., Wielebinski, R., Reuter, H.-P., Harnett, J. I., & Hummel, E. 1995, A&AS, 114, 147
Bajaja, E., Agüero, E., & Paolantonio, S. 1999, A&AS, 136, 179
Beck, R., Brandenburg, A., Moss, D., Shukurov, A., & Sokoloff, D. 1996, ARA&A, 34, 155
Beck, R. 2000, Phil. Trans. R. Soc. Lond. A., 358, 777
Beck, R. 2002, in Disks of Galaxies, ed. E. Athanassoula, et al., ASP Conf. Proc., 275, 331
Beck, R. 2004, Ap&SS, 289, 293
Beck, R., & Hoernes, P. 1996, Nature, 379, 47
Beck, R., Ehle, M., et al. 1999, Nature, 397, 324
Beck, R., Shoutenkov, V., Ehle, M., et al. 2002, A&A, 391, 83
Combes, F., Dupraz, C., Casoli, F., & Pagani, L. 1988, A&A, 203, L9
Condon, J. J. 1992, ARA&A, 30, 375
de Vaucouleurs, G., de Vaucouleurs, A., Corwin, H. G., et al. 1991, Third Reference Catalogue of Bright Galaxies (Berlin: Springer-Verlag)
Ehle, M., Beck, R., Haynes, R. F., et al. 1996, A&A, 306, 73
Englmaier, P., & Gerhard, O. 1997, MNRAS, 287, 57
Fan, Z., & Lou, Y. Q. 1997, MNRAS, 291, 91
Frick, P., Beck, R., Shukurov, A., et al. 2000, MNRAS, 318, 925
Garcia, A. M. 1993, A&AS, 100, 47
Han, J. I., Manchester, R. N., Berkhuijsen, E. M., & Beck, R. 1997, A&A, 322, 98
Harnett, J. I. 1984, MNRAS, 210, 13
Harnett, J. I., Wielebinski, R., Bajaja, E., Reuter, H.-P., & Hummel, E. 1991, PASA, 9, 258
Houghton, S. 1998, Ph.D. Thesis, University of New South Wales, Australia
Hummel, E., & Beck, R. 1995, A&A, 303, 691
Krause, F., & Beck, R. 1998, A&A, 335, 789
Lang, K. R. 1999, Astrophysical Formulae (Berlin: Springer-Verlag)
Lindblad, P. A. B., Lindblad, P. O., & Athanassoula, E. 1996, A&A, 313, 65
Longair, M. S. 1994, High Energy Astrophysics (Cambridge: Cambridge University Press)
Mihos, J. C., & Bothun, G. D. 1997, ApJ, 481, 741
Moss, D. 1998, MNRAS, 297, 860
Moss, D., Shukurov, A., Sokoloff, D., Beck, R., & Fletcher, A. 2001, A&A, 380, 55
Niklas, S., Klein, U., & Wielebinski, R. 1997, A&A, 322, 19
Piner, B. G., Stone, J. M., & Teuben, P. J. 1995, ApJ, 449, 508
Roberts, W. W., Huntley, J. M., & van Albada, G. D. 1979, ApJ, 233, 67
Rohde, R., & Elstner, D. 1998, A&A, 333, 27
Rohde, R., Beck, R., & Elstner, D. 1999, A&A, 350, 423
Ryder, S. D., & Dopita, M. A. 1993, ApJS, 88, 415
Ryder, S. D. 1995, ApJ, 444, 610
Ryder, S. D., Koribalski, B., Staveley-Smith, L., et al. 2001, ApJ, 555, 232
Sault, R. J., & Killeen, N. 1999, Miriad Users Guide, ATNF
Shukurov, A. 1998, MNRAS, 299, L21
Soida, M., Urbanik, M., & Beck, R. 1996, A&A, 312, 409
Sokoloff, D., Bykov, A., Shukurov, A., et al. 1998, MNRAS, 299, 189 (Erratum, MNRAS, 303, 207, 1999)
Woodings, S., Martin, R., Williams, A., Biggs, J., & Verveer, A. 1999, IAU Circ., 7316